

RED RUNAWAYS II: LOW MASS HILLS STARS IN SDSS STRIPE 82

YANQIONG ZHANG^{1,2}, MARTIN C. SMITH¹, JEFFREY L. CARLIN^{3,4}

¹Key Laboratory of Galaxies and Cosmology, Shanghai Astronomical Observatory, Chinese Academy of Sciences, 80 Nandan Road, Shanghai 200030, China

²Graduate University of the Chinese Academy of Sciences, No.19A Yuquan Road, Beijing 100049, China

³Rensselaer Polytechnic Institute, Troy, USA and

⁴LSST and Steward Observatory, 933 North Cherry Avenue, Tucson, AZ 85721, USA

Draft version March 5, 2024

ABSTRACT

Stars ejected from the Galactic centre can be used to place important constraints on the Milky Way potential. Since existing hypervelocity stars are too distant to accurately determine orbits, we have conducted a search for nearby candidates using full three-dimensional velocities. Since the efficacy of such studies are often hampered by deficiencies in proper motion catalogs, we have chosen to utilize the reliable, high-precision SDSS Stripe 82 proper motion catalog. Although we do not find any candidates which have velocities in excess of the escape speed, we identify 226 stars on orbits that are consistent with Galactic centre ejection. This number is significantly larger than what we would expect for halo stars on radial orbits and cannot be explained by disk or bulge contamination. If we restrict ourselves to metal-rich stars, we find 29 candidates with $[\text{Fe}/\text{H}] > -0.8$ dex and 10 with $[\text{Fe}/\text{H}] > -0.6$ dex. Their metallicities are more consistent with what we expect for bulge ejecta, and so we believe these candidates are especially deserving of further study. We have supplemented this sample using our own radial velocities, developing an algorithm to use proper motions for optimizing candidate selection. This technique provides considerable improvement on the blind spectroscopic sample of SDSS, being able to identify candidates with an efficiency around 20 times better than a blind search.

Subject headings: Galaxy:center; Galaxy:kinematics and dynamics; Galaxy:structure

1. INTRODUCTION

The presence of outliers in the velocity distribution of nearby stars has been known for many years. Traditional ‘runaway’ stars, with peculiar velocities typically greater than 40 km/s, constitute approximately 30% of O- and B-type stars in the solar neighborhood (e.g., Gies 1987; Stone 1991; Tetzlaff et al. 2011). Most runaway stars are ejected from the Galactic plane shortly after their formation (Ramspeck et al. 2001).

In 2005, a late B-type star was discovered in the outer halo having a heliocentric radial velocity of 853 ± 12 km/s, which is significantly in excess of the Galactic escape speed at that location (Brown et al. 2005). Such stars are called ‘hypervelocity stars’ (HVSs; for a recent review see Brown 2015). Hills (1988) predicted the existence of HVSs, suggesting that they can form via tidal disruption of a stellar binary by the central supermassive black hole of the Milky Way. In this scenario, one of the binary stars is captured by the black hole, while the other is ejected, often at an extremely high velocity. To-date around 30 A/B/O-type unbound HVSs have been found (see Brown 2015). Such stars can be used to probe star formation in the Galactic center or constrain the potential of the Milky Way (e.g. Gnedin et al. 2005).

The ejection rate of HVSs has been calculated in various studies and has been used to investigate the properties of the progenitor systems. For example, the work of Zhang et al. (2013) consider models that inject binaries from nuclear stellar disks adopting different stellar mass functions. They compare these to the observed S-stars in

the Galactic Center and the B-type HVSs in the Galactic halo. The models that best match the set of observations have HVS ejection rates of 10^{-4} to 10^{-5} per year. Similar studies modeling the properties of HVS have been carried out, for example Kenyon et al. (2014) or Rossi et al. (2014), and even the possibility of an LMC origin has been considered (Boubert & Evans 2016).

Most other mechanisms are not expected to produce such high-velocity stars, such as three-body interactions in the disk (Poveda et al. 1967) or super-nova kicks (Blaauw 1961). Recent works have made predictions for the ejection velocities from these scenarios, showing that velocities in excess of a few hundred km/s are unlikely (e.g. Portegies Zwart 2000; Perets & Šubr 2012). Some studies argue otherwise, for example Tauris (2015) has claimed that asymmetric supernovae can produce runaway stars with velocities as high as 1,000 km/s, but this work cautions that more detailed population synthesis studies are required to make robust predictions for the rates of such ejecta.

Although all currently known HVSs are young (O-/B-/A-type) stars, given the slope of the initial mass function one may expect many more older, low-mass HVSs (Kollmeier & Gould 2007). In an early attempt to find these, Kollmeier et al. (2010) used the non-detection of low-mass HVS in the Sloan Digital Sky Survey (SDSS) to place an upper limit on their formation rate, concluding that the ejection rate of unbound F/G-type stars is no more than 30 times larger than that of B-type ejecta.

More-recently Palladino et al. (2014) found 20 low mass G- and K-type HVSs candidates from SDSS by incorporating proper motions, something which Kollmeier

et al. avoided. Half of these candidates exceeded their corresponding escape velocity with at least 98% probability, but as none of the orbits were consistent with Galactic center ejection their nature remained unclear. However, in the following year, Ziegerer et al. (2015) reanalyzed the proper motions for 14 of these and found that they are all, in fact, bound to Galaxy and the initial (incorrect) HVS classification was due to flawed proper motions. Other low-mass hyper-velocity candidates have been claimed (e.g. Li et al. 2012), but these may also be subject to spurious proper motions.

Having realized the importance of reliable proper motions, Vickers et al. (2015) carried out a more cautious study of the runaway population of low-mass stars in SDSS including more stringent proper motion cuts. They were able to detect a number of high-velocity runaway stars, but all of their hyper-velocity candidates were marginal detections (with only one greater than 1σ). Therefore, in effect, this result is in agreement with Kollmeier et al. (2010).

In this paper we continue the hunt for low-mass ejecta in SDSS, focusing on high-quality proper motions and developing new techniques for optimizing future searches. Note that the term HVS refers to stars that have been ejected from an interaction with the supermassive black hole *and* have velocities in excess of the escape speed at their present location. However, since we are interested in all stars that have been ejected by the Hills mechanism, regardless of whether or not they are bound to the Milky Way, we follow Vickers et al. (2015) and use the term Hills star.

The outline of our paper is as follows. In Section 2 we describe the SDSS Stripe 82 data used in our analysis. In Section 3 we use SDSS spectroscopy to identify 226 Hills candidates, 29 of which are metal-rich. In Section 4 we add our own data from the Palomar telescope and identify one Hills candidate with $[\text{Fe}/\text{H}] \sim -0.4$ dex. In Section 5 we discuss the possible sources of contamination, most importantly halo stars on radial orbits. We conclude in Section 6.

2. DATA AND INITIAL QUALITY CUTS

2.1. Photometry

In order to identify Hills stars reliably, one of the most important ingredients is a robust catalog of proper motions. Because of this, we have chosen to focus our study on the Sloan Digital Sky Survey (SDSS) Stripe 82 region. This is a narrow 2.5 deg wide stripe along the celestial equator in the south Galactic cap, covering 250 deg² around $l \sim 60$ to 190 deg, $b \sim -20$ to -60 deg. This stripe has been repeatedly imaged by SDSS over 7 years allowing for studies of the variable sky and identification of many kinds of transient phenomena (e.g. Sesar et al. 2007; Watkins et al. 2009). This dataset has also been used to construct high accuracy proper motion catalogs (Bramich et al. 2008; Koposov et al. 2013). The Bramich et al. (2008) catalog is complete down to $r \sim 21.5$ mag, making it one of the deepest large-area catalogs of its kind. The catalog was subsequently revised in Koposov et al. (2013), removing some low-level systematics and improving the uncertainties by using quasars as a reference frame. The resulting catalog has a precision of around 2 mas yr⁻¹ and negligible sys-

tematic errors (~ 0.1 - 0.2 mas yr⁻¹). These catalogs have been exploited to hunt for white dwarfs (Vidrih et al. 2007) and wide binaries (Quinn & Smith 2009), and analyze the kinematic properties of Galactic disk and halo stars (Smith et al. 2009b,a, 2012).

We also need good photometry, so that we can estimate distances using the photometric relations from Ivezić et al. (2008) and Bond et al. (2010a). Our photometry mainly comes from the Annis et al. (2014) catalog, where the multiple Stripe 82 epochs have been co-added to result in a high precision catalog (e.g. 0.5% photometry in g, r, i and 1% in u). The u -band was sometimes problematic and there are cases where no u -band magnitudes are reported; for these stars we have used the standard single-epoch SDSS u -band photometry (Abazajian et al. 2009), although we have not included any stars with error greater than 0.2 mag.

We first de-redden our photometry using the maps of Schlegel et al. (1998). To ensure good quality photometry and astrometry we only use stars with magnitudes in the range 15 to 21 for all u, g, r, i -bands. Second, we insist that the mean object type ≥ 5.7 . This requires an object to be classified as a star in ≥ 90 per cent of epochs. This is less than 100 per cent in order to retain objects that have been misclassified in a limited number of epochs due to problems with the SDSS star-galaxy separation algorithm. In the Bramich et al. (2008) catalog, this occurs particularly in the final season, when observations were not exclusively taken in photometric conditions. Third, we insist that the proper motion error is less than 4 mas yr⁻¹ to clean any objects with problematic astrometry. Then we identify objects on the stellar locus using the following cuts (Ivezić et al. 2008):

$$0.7 < (u - g)_0 < 2.0, \quad (1)$$

$$-0.25 < (g - r)_0 - 5(u - g)_0 < 0.05, \quad (2)$$

$$-0.2 < 0.35(g - r)_0 - (r - i)_0 < 0.1. \quad (3)$$

where the subscript ‘0’ denotes a color that has been extinction corrected using the maps of (Schlegel et al. 1998).

Table 1 shows the number of stars passing these photometric cuts. A total of 249,901 stars pass these criteria, of which 36,869 use the SDSS single-epoch u -band magnitude (with the rest having u -band magnitudes from the Annis et al. 2014 co-add).

2.2. Spectroscopy

To complement these proper motions, we need spectroscopy to obtain radial velocities. We first obtain these from existing SDSS spectroscopy, then later supplement this sample with our own observations (see Section 4).

The SDSS project, and in particular its Galactic extension SEGUE (Yanny et al. 2009), have obtained spectra for hundreds of thousands of stars. Stellar atmospheric parameters have been determined by the Sloan Stellar Parameter Pipeline data product (SSPP; see Lee et al. 2008a), and radial velocities found via ELODIE template matching. We have cross-matched our photometric sample with the SDSS DR10 spectroscopic catalogue, and found that $\sim 5.7\%$ have suitable spectra – defined as those with SSPP flag set to ‘nnnn’, which implies that

there are no cautionary signs and the stellar parameters should be well determined (Lee et al. 2008b). In this work we limit ourselves to spectra with $S/N \geq 10$ and apply the following quality cuts: $\delta v_{\text{helio}} < 30$ km/s, $\delta \log(g) < 0.5$ dex, $\delta[\text{Fe}/\text{H}] < 0.5$ dex.

Our analysis focuses on main-sequence stars, so we reject giant contamination by removing all stars with $\log(g) < 3$ dex¹. A total of 13,538 stars pass these cuts (see Table 1). The median uncertainties on the resulting sample are 2.1 km/s, 0.08 dex and 0.04 dex, for δv_{helio} , $\delta \log(g)$, and $\delta[\text{Fe}/\text{H}]$, respectively. These uncertainties, which are those reported by the SSPP pipeline (Lee et al. 2008b), are estimates of the internal precision; if we fold in external errors (Allende Prieto et al. 2008), then the total uncertainties are likely to be around 3.3 km/s, 0.22 dex and 0.12 dex, for δv_{helio} , $\delta \log(g)$, and $\delta[\text{Fe}/\text{H}]$, respectively. For our calculations of the location and velocity of the last disk crossing the main source of uncertainty comes from the proper motions, and so the fact that these internal spectroscopic uncertainties may be underestimated is of little consequence.

2.3. Distances

To determine the full six-dimensional phase-space for each star, we need to estimate distances. We do this using the relations presented in Ivezić et al. (2008). These relations are valid for dwarf stars in the color range $0.3 \leq (g - i)_0 \leq 4.0$, so we first reject all stars outside this range (note that we remove giant stars by enforcing $\log(g) < 3$ dex; see Section 2.2). We then estimate the distance using the color-magnitude relation given in equations (A1), (A4) and (A5) of Ivezić et al. (2008). We also incorporate the $[\text{Fe}/\text{H}]$ dependence given in their equation (A2), where we use the metallicity determined from the SDSS spectra. Smith et al. (2012) noted that the turn-off correction of Ivezić et al. (2008) is not ideal for general disk stars. They concluded that for the magnitude range $0.3 < (g - i)_0 < 0.6$ a better choice is to have no turn-off correction and to simply increase the uncertainty (equation A1 of Smith et al. 2012). We adopt this approach for our present study.

Combining the uncertainty in the Ivezić et al. (2008) relation with the error on $[\text{Fe}/\text{H}]$, Smith et al. (2012) found that for their Stripe 82 sample the median distance error was 10.7%. Therefore in our current work we simplify our calculation by assuming all stars have a distance error of 10%. Our distances are mostly in the range 0.5 to 5 kpc, although there are a small number of stars further out. This gives us a final sample of 13,170 dwarfs with SDSS spectra (see Table 1).

3. IDENTIFYING CANDIDATE HILLS STARS

3.1. Calculation of the last disk crossing

Given the position and velocity of each star in our sample, we can integrate the orbit back through time to calculate the last disk crossing. Clearly Hills stars should have orbits whose last disk crossing intersects the Galactic center. We use potential 2b from Dehnen & Binney (1998), which is a reasonable match to the more-recent

model of McMillan (2011). Dehnen & Binney’s model consists of three exponential disk components (corresponding to the inter-stellar medium, the thin and thick disks), together with a spherical bulge and halo. This is then fit to a variety of observations in order to constrain the parameters of their model.

Throughout this work we use a right-handed Cartesian coordinate system centered on the Galactic Center (GC), with the x-axis pointing from the Sun to the GC, the y-axis pointing in the direction of rotation and the z-axis pointing towards the Northern Galactic Pole. We assume that the motion of the local standard of rest (LSR) is 238 ± 9 km/s, the velocity of the Sun with respect to the LSR is $(14.0 \pm 1.5, 12.24 \pm 0.47, 7.5 \pm 0.3)$ km/s, and the Sun lies at $x = -8.27 \pm 0.29$ kpc (Schönrich 2012).

Orbits are calculated for every star in our sample by reversing their velocities and running them through potential 2b for 1 Gyr with a time-step of 1 Myr resolution. The choice of a 1 Gyr integration time is to ensure we find crossings where possible. When an orbit crosses the Galactic plane, a linear interpolation between the calculation steps before and after the crossing is used to find the exact coordinates and velocities of the crossing point. We assume here that the most-recent crossing time was the point where the object was ejected, if it was ejected. We refer to this most-recent crossing location as the ‘crossing position’ ($\mathbf{r}_{\text{cr}} = [x_{\text{cr}}, y_{\text{cr}}, 0]$), and the speed at this point as the ‘crossing velocity’ ($|\mathbf{v}_{\text{cr}}|$).

Uncertainties in the crossing position are calculated using a Monte Carlo approach. We assume all observational errors are Gaussian and generate 400 realizations for each star in our sample. We account for all sources of uncertainty, namely the helio-centric distance, radial velocity, proper motion, together with uncertainties in the LSR and solar radius.

For each star we use the distribution of $(x_{\text{cr}}, y_{\text{cr}})$ from our 400 realizations to estimate the crossing radius and uncertainty as follows,

$$r_{\text{cr}} = |\mathbf{r}_{\text{cr}}| = \sqrt{\langle x_{\text{cr}} \rangle^2 + \langle y_{\text{cr}} \rangle^2} \quad (4)$$

$$\delta r_{\text{cr}} = \frac{\sqrt{\langle x_{\text{cr}} \rangle^2 \sigma(x_{\text{cr}})^2 + \langle y_{\text{cr}} \rangle^2 \sigma(y_{\text{cr}})^2 + \langle x_{\text{cr}} \rangle \langle y_{\text{cr}} \rangle \sigma(x_{\text{cr}}, y_{\text{cr}})}}{r_{\text{cr}}} \quad (5)$$

where angle brackets denote the mean of the realizations, $\sigma(X)$ denotes the standard deviation and $\sigma(X, Y)$ denotes the square root of the covariance. Note that since the distribution of r_{cr} values does not follow a normal distribution, it would be incorrect to take the standard deviation to represent the uncertainty. The correct uncertainty on this quantity can be obtained through error propagation, as given in the above equation.

For the crossing velocity we take the value corresponding to the crossing radius calculated from equation (4). We do this, rather than use the mean from our realizations, because v_{cr} and r_{cr} are strongly correlated. One consequence of this approach is that if there are any Hills stars in our sample, this value of v_{cr} will significantly underestimate the true ejection velocity; even if the probability distribution function of r_{cr} indicates that it is consistent with zero, our adopted value of r_{cr} can never be precisely zero (due to an offset from observational errors), and hence the corresponding v_{cr} will be lower than

¹ Even though this is not a very strong cut, it is unlikely our final sample contains giant contamination as our Hills candidates all have significant proper motions, which would not be the case for distant giant stars.

TABLE 1
THE NUMBER OF SDSS HILLS CANDIDATES AFTER THE RESPECTIVE CUTS.

Cut	Section	Description of cut	Number of objects
1	2.1	Bright stars passing our photometric cuts	249,901
2	2.2	High-quality SDSS stellar spectra	14,174
3	2.2	Main-sequence stars ($\log(g) \geq 3$ dex)	13,538
4	2.3	Color within range of the photometric parallax relation	13,170
5	3.2	SDSS Hills candidates	226
6	3.2	Metal-rich SDSS Hills candidates (SHCs)	29

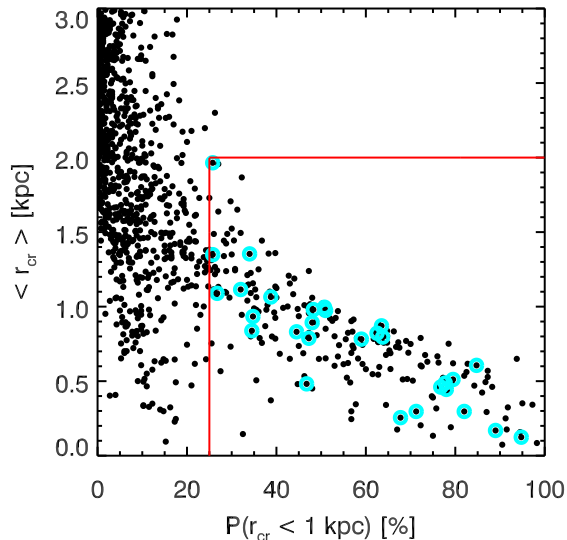


FIG. 1.— This figure shows the mean value of the last disk crossing radius (r_{cr}) versus the probability that the last disk crossing radius is less than 1 kpc for all main-sequence stars with good SDSS spectroscopy and distances in Stripe 82 (Cut 4 from Table 1). Cyan points show our 29 metal-rich Hills candidates and the red line shows our selection boundary.

the ejection velocity corresponding to $r_{\text{cr}} = 0$.

Once we have identified our sample of Hills candidates, we repeat this procedure at higher resolution (using 5,000 realizations) in order to improve our estimates. Throughout this paper we calculate probabilities of crossing location using the actual distributions of our realizations; the above errors are only quoted in the table of candidates.

3.2. Candidates from SDSS spectroscopy

We identify good candidates using the probability distributions for r_{cr} from the Monte Carlo resamples. We first obtain an initial sample of Hills candidates by rejecting all stars with $|\langle r_{\text{cr}} \rangle|$ greater than 2 kpc and only retaining stars with $P(r_{\text{cr}} < 1\text{kpc}) > 25\%$. These two cuts are illustrated in Fig. 1. This latter cut is important as it removes stars with crossing positions that are highly uncertain or unlikely to be coincident with the Galactic centre.

We do not expect all of these to be genuine Hills stars, with the main source of contamination being halo stars on radial orbits. To remove halo contamination we impose a cut on the metallicity, requiring $[\text{Fe}/\text{H}] > -0.8$ dex. Note that the metallicity distribution of the halo is well described by a normal distribution with mean -1.46 dex and dispersion 0.3 dex (Ivezić et al. 2008; Bond et al. 2010a), while bona-fide Hills stars are expected to have been born in the central parts of the galaxy and should therefore be metal-rich. This cut should remove most

halo contamination, but we leave a detailed discussion of halo contamination to Section 5.

A total of 29 Hills candidates pass this metallicity cut, and we label these SDSS Hills Candidates (SHC1–29). The properties of these 29 stars are shown in Figure 2, alongside our larger sample of 226 candidates and the full spectroscopic sample of 13,170 dwarfs (see Table 1). Clearly most stars in the full sample are regular disk stars, with metallicities around -0.5 dex and radial velocities around 0 km/s. However, most of 226 Hills candidates are metal-poor, confirming our suspicion that halo stars are an important source of contamination. The far-right panel of Fig. 2 shows the current spatial distribution of these samples, where because of the orientation of Stripe 82 these objects are below the plane and are at Galacto-centric radii of between 6 and 10 kpc. The distribution is fairly homogeneous across the Stripe 82 field. The center-left panel shows the radial velocity distribution. The Hills candidates have high radial velocities, but not exceptionally high, i.e. they are similar to other high velocity stars in the solar neighborhood. This means that one cannot identify such Hills stars using radial velocity alone, unlike the previously detected unbound hyper-velocity stars (e.g. Brown et al. 2014), and all of our candidates are bound to the Milky Way potential. Because of the orientation of the orbits in our sample, most of these Hills candidates have negative radial velocities, i.e. are moving towards the Sun. The center-right panel shows the distribution of crossing velocities². The crossing velocities of our Hills candidates are mostly around 450 km/s or more, which is necessary for them to make the journey from the central parts of the Galaxy to the Solar neighborhood. As discussed in Section 1, such ejection speeds are unlikely to be obtained through other mechanisms. Perets & Šubr (2012) showed that dynamical (three-body) encounters in clusters are unlikely to produce ejection velocities of hundreds of km/s, especially for low-mass stars (see Fig. 3 of their paper). The likelihood of this occurring from a supernovae binary ejection is also negligible; velocities of up to 200 or 300 km/s are possible, but unlikely for low-mass stars like the ones we consider here (e.g. Fig. 6 of Portegies Zwart 2000).

Table 2 lists the properties of our 29 metal-rich Hills candidates. The proper motions and g -band magnitudes are obtained from SDSS Stripe 82 data (Koposov et al. 2013; Annis et al. 2014). The metallicities and heliocentric radial velocities come from SDSS spectroscopy. As can be seen from their total velocities, all are bound to

² As explained in Section 3.1, this is the velocity corresponding to the crossing radius calculated from equation (4) and, if these are bona-fide Hill stars, then their true ejection velocities would be significantly greater.

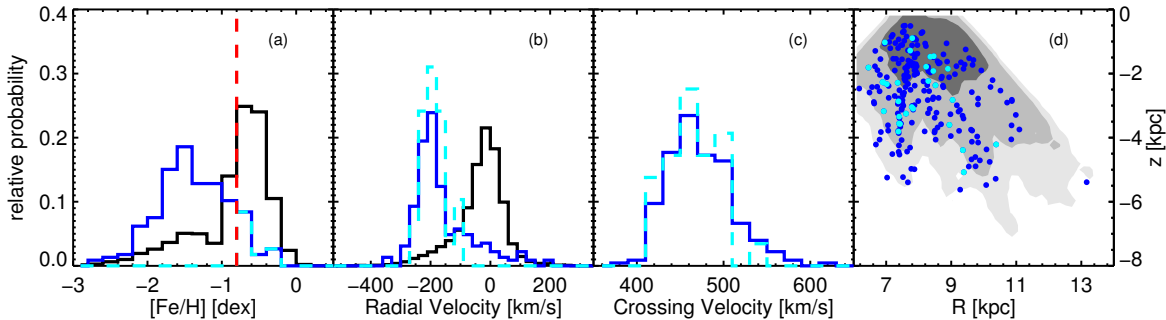


FIG. 2.— The various properties of our Hills samples: (a) the metallicity, (b) radial velocity, (c) velocity at last disc crossing and (d) current spatial distribution in Galactocentric cylindrical coordinates. Black lines correspond to the entire sample of SDSS dwarfs (Cut 4 from Table 1), the blue lines correspond to the full sample of 226 Hills candidates (Cut 5) and the cyan lines to the 29 metal-rich candidates ([Fe/H] > -0.8 dex; Cut 6). In panel (d) we use contours to denote the distribution of the full spectroscopic sample, using dark grey for 1σ , grey for 2σ , and light grey for 3σ .

the Galaxy, assuming the escape speed is 500–600 km/s (Smith et al. 2007; Piffl et al. 2014).

The first ten rows of Table 2 show our best Hills candidates, in that their metallicities are all greater than -0.6 dex (and hence less-likely to be halo stars; see Section 5 for further discussion on this point). Their typical last crossing velocities are larger than 400 km/s and for most the last crossing radii are within a kpc of the Galactic center. In Figure 3, we show the probability distribution for the crossing position of the nine most metal-rich Hills candidates. The uncertainties come from our Monte Carlo calculation (see Section 3.1). For five of these nine stars (SHC1, SHC3, SHC4, SHC6 and SHC8) the Galactic center is within 1σ of the crossing position and hence they are especially deserving of further study. Amongst our larger sample of 29 metal-rich SDSS Hills candidates, the GC lies within 1σ of the crossing position for around half of all candidates. The distributions of last disk crossing location for these candidates are presented in the Appendix.

4. OPTIMIZING CANDIDATE SELECTION FROM PROPER MOTION SURVEYS

The efficiency of detecting Hills candidates from a blind spectroscopy survey (i.e. one with no preferential targeting of Hills candidates) is clearly limited. The SDSS spectroscopic catalogue described above had an efficiency of only around 0.1%, with 10-20 Hills candidates coming from a total of 13,170 stellar spectra in the Stripe 82 region. In this section we describe an approach to optimize the search efficiency by utilizing proper motion information, then apply this technique to obtain candidates using spectroscopy from the Palomar 200-inch telescope.

4.1. Target selection

We again base our target selection on the high-quality Stripe 82 proper motions (Bramich et al. 2008; Koposov et al. 2013). Targets are selected with SDSS g -band magnitudes between $16 < g < 19$, which balances our desire to observe many candidates with the need for sufficient S/N to measure reliable line-of-sight velocities and metallicities.

As can be seen in the previous section (e.g. the top-left panel of Figure 2), most of our Hills candidates are metal-poor ([Fe/H] $\lesssim -1.0$), but stars that have been ejected from the Galactic center are expected to be relatively metal-rich. We thus use photometric metallicity

relations to focus our search on metal-rich stars, utilizing the relations presented in Ivezić et al. (2008) and Bond et al. (2010a). This method is calibrated for F- and G-type main-sequence stars, which we select by applying a color cut of $0.2 \leq (g-r)_0 \leq 0.6$ to the Stripe 82 catalog; this is in addition to the cuts described in Section 2.1 and Section 2.3 that are imposed to deliver stars on the stellar locus with good photometry. We choose to reject all stars with photometric metallicity [Fe/H] < -0.6, leaving a total of 21,052 stars that pass all of these cuts.

Distances are calculated using the approach described in Section 2.3. Because the errors on individual photometric metallicities are larger than spectroscopic measurements, the errors in our derived distances are correspondingly larger at around 20%. We use these distances to estimate the current 3D positions and tangential velocities of all stars satisfying the above cuts, using the same approach as described in Section 2.3.

To select the best candidates for Palomar observations, we simulate the orbits of all 21,052 stars for a range of radial velocities. In the top-right panel of Figure 2, it can be seen that most of the radial velocities for our Hills candidates are negative. If we calculate the last disk crossing (i.e. potential ejection position) for each star as a function of the unknown radial velocity and focus on stars with minimum crossing position less than 0.5 kpc, we find that the minimum crossing position almost always occurs when the radial velocity lies in the range -450 to -50 km s⁻¹ (only 1% of these stars have velocities outside this range). We use this velocity range in the following analysis.

For each of our 21,052 stars, we calculate 400 Monte Carlo realizations of the orbit. We do this following the approach described in Section 3.1, incorporating errors on all observable quantities (helio-centric distance, proper motion, LSR and solar radius), but since we do not know the radial velocity we choose this uniformly within the range [-450, -50] km s⁻¹. An example is illustrated in Figure 4, where each point corresponds to the last disk crossing location for an individual Monte Carlo realization of the orbit³. Potential Hills candidates can be identified using this crossing track, with good candidates being those for which the track intersects the Galactic centre (such as this example).

³ Note that for the sake of clarity this figure uses 1000 realizations. Our candidates were selected using only 400 realizations in order to minimize computational time.

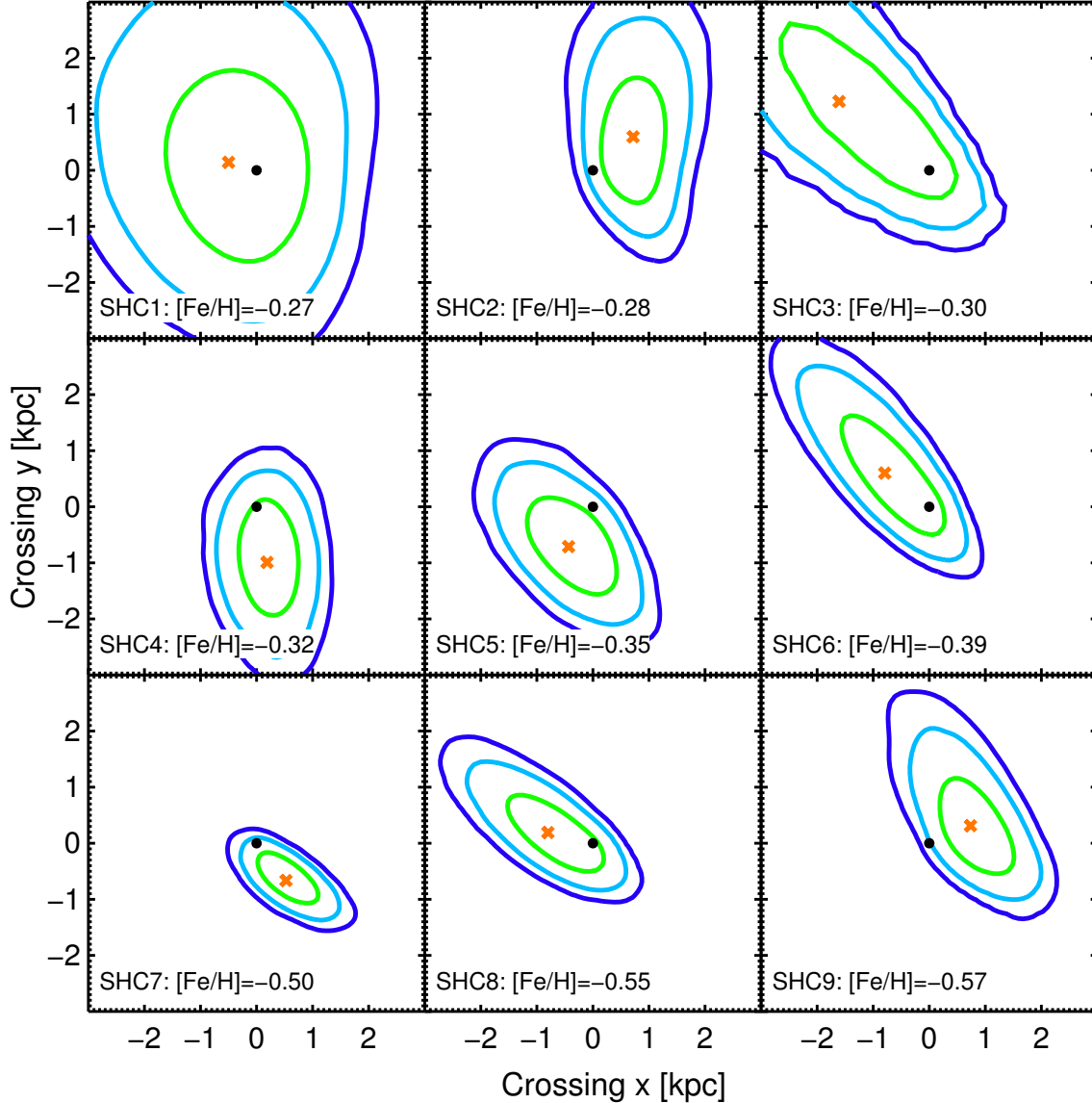


FIG. 3.— This figure shows the last disk crossing position for our nine most metal-rich SDSS Hills candidates (i.e. with $[Fe/H] \geq -0.57$ dex). The green, cyan and blue lines correspond to 1σ , 2σ and 3σ , respectively. The orange crosses show the crossing position if we do not account for observational errors. The black dot shows the position of Galactic center. The remaining candidates are shown in Fig. 9.

We classify the strength of these candidates using two quantities derived from these Monte Carlo simulations: $N_{1.0}$ is the number of realizations for which the last disk crossing position lies within 1 kpc of the GC, and $N_{0.5}$ is number of realizations within 0.5 kpc of the GC. We define two sets of candidates, where the second is included to provide additional candidates at high Right Ascension, compensating for the fact that most candidates are at low Right Ascension and would not be observable for the whole night during our run.

- Main targets: $N_{1.0} > 124$ ($\sim 30\%$), $N_{0.5} > 58$ ($\sim 15\%$), $[Fe/H] > -0.45$;
- High-RA targets: $RA > -30^\circ$, $N_{1.0} > 99$ ($\sim 25\%$), $N_{0.5} > 39$ ($\sim 10\%$), $[Fe/H] > -0.6$.

We select 60 main and 16 high-RA targets. Two good targets were later rejected because they lie close to bright stars and would be difficult to observe.

4.2. Palomar 200-inch observations

Observations were carried out on the nights of 29-31 August 2014 using the Double Spectrograph (DBSP; Oke & Gunn 1982) on the Hale 200-inch (P200), with time awarded from China’s Telescope Access Program. DBSP splits the light by use of a dichroic, allowing simultaneous observation of blue and red channel spectra. For our purposes, we used the D55 dichroic to place the transition at $\sim 5500 \text{ \AA}$. All observations used a $128''$ -long slit with a width of 1.0 arcsec, with typical seeing on all three nights of $\sim 0.8 - 1.2''$. In the blue channel, we used the 600 line/mm grating (600/4000) centered at $\sim 4500 \text{ \AA}$, and the 600 line/mm grating (600/10000) centered at $\sim 7200 \text{ \AA}$ in the red channel. This set up achieved resolutions of $R \equiv \frac{\lambda}{\Delta\lambda} \sim 1800$ and $R \sim 2400$ at the positions of the hydrogen Balmer ($H\beta$ and $H\alpha$) lines in the blue/red channels, respectively, with nearly con-

TABLE 2
THE PROPERTIES OF OUR METAL-RICH ($[\text{Fe}/\text{H}] > -0.8$) HILLS CANDIDATES.

name	IAU name	μ (mas/yr)	g (mag)	$[\text{Fe}/\text{H}]^a$ dex	d_{helio}^a kpc	v_{helio}^a km s $^{-1}$	v_{tot} km s $^{-1}$	v_{cr} km s $^{-1}$	r_{cr} kpc	$P(r_{\text{cr}} < 1\text{kpc})$ %
SHC1	J014305.79-003903.8	10.33 \pm 1.09	18.53	-0.27	4.83	-104.8 \pm 3.9	258.7	509.8	0.50 \pm 0.86	47.8
SHC2	J004614.45-010346.9	16.13 \pm 1.09	18.40	-0.28	3.14	-152.0 \pm 2.6	284.4	450.0	0.94 \pm 0.36	50.0
SHC3	J221807.24+005439.8	9.12 \pm 1.16	19.02	-0.30	5.17	-229.1 \pm 3.9	320.1	410.4	2.05 \pm 1.57	24.9
SHC4	J001740.99-002759.1	10.03 \pm 0.83	18.28	-0.32	4.07	-98.6 \pm 3.2	217.3	459.5	1.00 \pm 0.36	46.8
SHC5	J213915.13+011006.1	8.84 \pm 1.53	18.30	-0.35	3.98	-150.6 \pm 2.2	224.6	489.9	0.82 \pm 0.32	49.4
SHC6	J220317.08+010539.7	9.98 \pm 1.69	17.95	-0.39	3.51	-195.1 \pm 2.1	256.2	427.8	0.98 \pm 0.82	51.6
SHC7	J221331.35+005508.2	14.73 \pm 0.74	16.79	-0.50	1.89	-207.5 \pm 1.1	245.8	440.8	0.84 \pm 0.41	65.9
SHC8	J220347.45-010526.0	29.28 \pm 0.94	17.14	-0.55	1.34	-196.6 \pm 2.0	270.3	442.1	0.82 \pm 0.62	62.1
SHC9	J223257.10+002939.5	7.69 \pm 0.89	18.65	-0.57	4.46	-246.5 \pm 5.1	295.3	455.0	0.80 \pm 0.25	55.0
SHC10	J221952.86-011254.2	8.29 \pm 0.99	18.67	-0.59	4.03	-173.3 \pm 4.1	234.6	421.2	1.12 \pm 0.41	25.3
SHC11	J221738.85+003322.3	6.09 \pm 1.49	19.18	-0.61	4.83	-244.8 \pm 3.5	281.7	431.0	1.43 \pm 0.91	29.3
SHC12	J002458.60-010832.5	7.41 \pm 1.11	18.08	-0.64	5.69	-142.6 \pm 6.9	245.4	476.3	0.81 \pm 0.76	35.7
SHC13	J005845.36+005346.9	18.60 \pm 1.02	17.61	-0.65	2.10	-159.3 \pm 1.8	244.2	451.0	0.94 \pm 0.20	34.9
SHC14	J221711.45+001937.6	7.73 \pm 1.44	19.53	-0.66	5.49	-231.4 \pm 7.5	306.7	459.5	0.83 \pm 1.22	46.5
SHC15	J222229.85-002903.3	7.10 \pm 1.43	19.68	-0.68	4.99	-224.8 \pm 5.5	280.7	499.2	0.27 \pm 0.35	69.5
SHC16	J205250.90+003453.6	6.32 \pm 1.64	18.52	-0.68	4.08	-233.0 \pm 4.0	263.0	495.1	0.51 \pm 0.57	78.7
SHC17	J235508.19+005619.5	17.71 \pm 0.94	16.83	-0.69	2.24	-197.4 \pm 2.1	272.9	432.7	1.09 \pm 0.68	39.6
SHC18	J213412.37-004311.0	8.08 \pm 1.04	18.09	-0.70	3.87	-204.3 \pm 2.2	252.3	451.9	0.51 \pm 0.58	77.9
SHC19	J214714.91-000227.3	5.23 \pm 1.73	19.32	-0.71	5.14	-198.4 \pm 6.1	235.7	474.0	0.27 \pm 0.72	67.1
SHC20	J001327.34-010136.5	26.97 \pm 0.64	16.40	-0.72	1.65	-217.9 \pm 2.0	303.0	497.9	0.43 \pm 0.76	76.8
SHC21	J232728.65+005409.6	20.35 \pm 0.83	17.95	-0.72	2.17	-158.1 \pm 2.1	262.3	472.3	0.59 \pm 0.28	86.3
SHC22	J003525.74-010942.1	9.48 \pm 1.12	18.87	-0.74	4.89	-161.1 \pm 5.9	272.7	441.0	1.45 \pm 1.20	24.3
SHC23	J225448.69-005430.2	7.75 \pm 0.96	19.05	-0.76	3.95	-182.1 \pm 2.2	232.8	452.9	0.91 \pm 0.37	43.5
SHC24	J213137.16+005736.7	6.78 \pm 1.65	19.27	-0.76	4.04	-225.9 \pm 6.1	260.5	472.4	0.46 \pm 0.09	76.0
SHC25	J234839.28+010320.3	25.04 \pm 1.73	17.40	-0.76	1.74	-153.5 \pm 2.2	257.2	503.4	0.16 \pm 0.07	91.2
SHC26	J204555.46-004653.3	9.13 \pm 1.66	17.04	-0.77	2.38	-222.9 \pm 2.0	245.5	427.5	1.09 \pm 0.47	33.7
SHC27	J233657.12-002138.7	14.77 \pm 0.90	17.43	-0.77	2.64	-209.0 \pm 1.8	279.0	490.5	0.33 \pm 0.56	80.2
SHC28	J224722.50+000802.0	10.93 \pm 0.93	18.52	-0.78	4.00	-187.1 \pm 2.2	279.1	451.8	0.83 \pm 0.22	61.5
SHC29	J235446.02+010819.4	19.53 \pm 0.68	17.09	-0.80	2.77	-107.5 \pm 2.6	278.2	540.2	0.11 \pm 0.06	94.6
PHC1	J225957.20+000543.8	8.20 \pm 1.07	18.59	-0.40	4.10	-124.4 \pm 10.0	202.2	393.89	1.70 \pm 0.46	3.22
PHC2	J225826.60+005013.6	13.44 \pm 0.72	18.20	-0.33	3.30	-79.1 \pm 2.4	224.6	358.62	2.58 \pm 0.34	0.00
PHC3	J231828.40-004040.6	18.02 \pm 1.06	17.74	-0.23	2.72	-203.3 \pm 5.9	308.8	430.91	1.74 \pm 1.71	25.41
PHC4	J214056.00+010020.0	22.65 \pm 1.15	18.20	-0.22	2.82	-194.0 \pm 5.0	358.7	510.16	1.34 \pm 0.42	11.85
PHC5	J222624.50-011416.0	8.54 \pm 0.90	18.40	-0.22	4.48	-70.4 \pm 2.4	194.6	357.13	2.84 \pm 0.45	0.02

Notes: SHC1–26 are candidates with SDSS spectroscopy (Sections 2 and 3), while PHC1–5 have P200 spectroscopy (Section 4). The typical distance errors are around 10–15%. Metallicity errors are around 0.1 dex for the SHC candidates and 0.2 dex for the PHC candidates. r_{cr} and v_{cr} denote the position and velocity at the last disk crossing (see Section 3.1).

tinuous wavelength coverage from $\sim 3000 - 8800 \text{ \AA}$. Each star was observed in two exposures, with typical exposure times ranging from 300 – 600 seconds, depending on the target magnitude.

DBSP separates spectra into two channels. With our setup, the blue band covers $\sim 3000 - 6020 \text{ \AA}$, and the red band $\sim 5520 - 8870 \text{ \AA}$. To reduce the targets spectra, we use the standard tasks in IRAF. We observed calibration lamps at the beginning of each night, including a HeNeAr lamp for the red channel and FeAr to fix the blue channel wavelength solution. However, after reducing the spectra, a check of sky lines with known wavelengths (including those at 4046.6 \AA , 4358.3 \AA , 5461.0 \AA , and 5577.3 \AA in the blue band, and 7750.6 \AA , 7821.5 \AA , 7913.7 \AA , 7993.3 \AA , 8344.6 \AA , 8382.4 \AA , 8399.1 \AA , 8430.1 \AA , 8452.3 \AA , and 8493.4 \AA in the red channel) shows offsets from their expected wavelengths. We thus correct each spectrum by this offset to place the sky lines at zero radial velocity.

For late-type stars, we predominantly use the calcium (Ca II) H and K lines (3933.7 \AA and 3968.5 \AA) to compute the average wavelength shift and obtain the best-fitting radial velocity in the blue band. In the red

band, we use the near-infrared Ca II triplet at 8498.0 \AA , 8542.1 \AA , and 8662.14 \AA to compute the average wavelength shift and obtain the best-fitting radial velocity. The mean errors for all spectra are less than 20 km s $^{-1}$ in the blue band and less than 10 km s $^{-1}$ in the red. We choose to adopt the red-band velocities because of the higher resolution and the fact that there are more sky lines in this region. For the fainter stars we took two separate exposures in the red band and use the average of the two velocities as our final value. The two separate measurements show good agreement within the expected observational errors.

As discussed above, metallicities are important for determining the likelihood that a star was ejected from the GC. We estimate metallicities using a method based on empirical fits to the behavior of $[\text{Fe}/\text{H}]$ as a function of spectral line indices. In particular, we measure the equivalent widths of spectral lines using bandpass and pseudo-continuum definitions defined by Worthey et al. (1994) for the low-resolution, Lick/IDS absorption line indices (Burstein et al. 1984; Faber et al. 1985; Gorgas et al. 1993). The set of standards defining our empirical calibration include the standard system of Schiavon

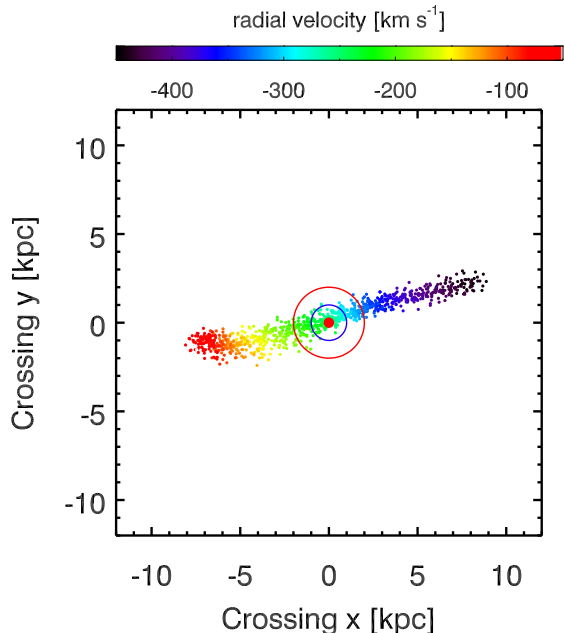


FIG. 4.— An example of a crossing track, showing how the location of the last disk crossing varies as a function of the radial velocity. Tracks which intersect the Galactic centre are candidate Hills ejecta. The width of the track is determined by the observational errors (mainly in the distance and proper motion) and the colors correspond to the radial velocity. The red point corresponds to the Galactic centre, and the blue and red circles denote 1.0 and 2.0 kpc radii, respectively.

(2007), and the MILES (Sánchez-Blázquez et al. 2006), the ELODIE.3.1 (Moultaka et al. 2004), and STELIB (Le Borgne et al. 2003) libraries of spectra. We derive surface fits to the behavior of $[\text{Fe}/\text{H}]$ as a function of the $\text{Fe}5270$ vs. $\text{H}\beta$ indices (which are primarily sensitive to iron and hydrogen abundances). In practice, we average a number of Fe indices from the spectra to derive an average iron index. The code recovers $[\text{Fe}/\text{H}]$ from high S/N spectra of stars with known metallicities with accuracy of ≤ 0.3 dex. This method has been used on low-resolution spectra of stars in the Sagittarius stream (Carlin et al. 2012), the Boötes III dwarf galaxy (Carlin et al. 2009), and the Anticenter Stream (Carlin et al. 2010), among others. We derive metallicities by running this algorithm on each of the spectra we obtained with DBSP and again adopt the values from the red part of the spectra. In general the agreement with the photometric metallicities is reasonable, with (as expected) a spread of around 0.4 dex. There are a couple of stars with spectroscopic values that are significantly more metal-poor than the photometric estimate, but as we describe below these are removed from our analysis.

4.3. Crossing positions and evaluation of success rate

Given the radial velocity and metallicity from the spectrum, we first refine our distance estimate using the spectroscopic metallicity and then compute the crossing position and velocity as before (see Section 3.1). We check the crossing position for the 76 targets and find that 8 have average crossing radii less than 3 kpc, but 3 of these have metallicity less than -0.8. We show the crossing positions for the remaining 5 metal-rich stars in Figure 5 and list their properties in Table 2. We label these candidates Palomar Hills Candidates (PHC1-5). The inset

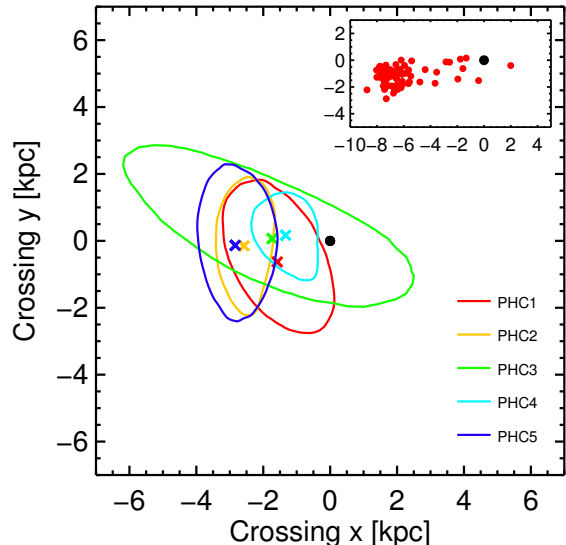


FIG. 5.— The distribution of last disk crossing location for our sample of P200 candidates. The black dot denotes the Galactic Center and the red dots in the inset show the crossing positions for all targets. The contours show the 3σ constraints on the crossing location for the five best candidates, i.e. with crossing radii less than 3 kpc and $[\text{Fe}/\text{H}] > -0.8$ dex.

of this figure shows the crossing position of all 76 stars; as expected most stars are on fairly circular orbits which last crossed the disk close to the solar radius.

For our best candidate, PHC3, the GC lies within 3σ of the last disk crossing, but the uncertainty on r_{cr} is large. For PHC4 the 3σ likelihood regions is close to the GC, and both v_{tot} and v_{cr} are large. However, its orbit does not appear to intersect the GC and so, although this may be a Hills candidate, it could only be so if there was a systematic error in one of the observed quantities (e.g. the distance or proper motion).

To compare our proper motion selection algorithm to the blind SDSS spectroscopic sample, we can see that we have one candidate with $r_{\text{cr}} < 2$ kpc, $P(r_{\text{cr}} < 1) > 25\%$ and $[\text{Fe}/\text{H}] > -0.6$. For our SDSS sample we have 10 stars which pass these criteria. So the proper motion selected sample has an efficiency of around $1/76 \sim 1.3\%$, while the SDSS sample has an efficiency of $10/13170 \sim 0.08\%$. We are in the regime of small number statistics, but there is undoubtedly a significant improvement when using our proper motion selected sample.

5. POSSIBLE SOURCES OF CONTAMINATION

For all of our Hills candidates, the current total spatial velocity is around 200 - 300 km s^{-1} , which is consistent with typical halo stars. It is known that halo stars are on radial orbits and so it is natural to wonder whether they may constitute a significant source of contamination in our sample. We now address this issue, together with other possible contaminants at the end of the section.

We can estimate the number of halo stars in our sample of 13,170 SDSS stars (Cut 4 in Table 1) by counting the fraction that are counter-rotating. We find that 1,038 stars are counter-rotating and, assuming these are all halo stars and that the halo has no significant net rotation, this implies that the total number of halo stars will be twice this, i.e. around 16%. We then estimate the distribution of peri-centric radii (r_{peri}) for a mock sample of halo stars, using the halo velocity dispersion

from [Smith et al. \(2009b\)](#). We take the positions of these mock halo stars from our observed sample of 13,170 stars, weighted by their halo probability as estimated from the density distribution of [Jurić et al. \(2008\)](#). We Monte Carlo this distribution to reduce statistical fluctuations and normalize so that the total number of stars matches the number predicted above.

The resulting r_{peri} distribution is shown with the black line in [Figure 6](#). The shaded region shows the 1σ uncertainty in the mock halo distribution, assuming Poissonian errors. The red line shows the observed distribution for our full sample of 226 Hills candidates, where the fall-off for large r_{peri} is simply due to the fact that we only considered candidates with small values of r_{cr} . Note that there is a clear excess in the observed distribution. If there were no Hills stars in this sample, then the observed number should not exceed the predicted halo distribution, so this indicates that some of the candidates should be real. This can also be seen in the inset, which shows the cumulative distribution of r_{peri} ; the observed distribution (red curve) is consistently in excess of the expectations from our mock halo distribution at a level of around 5σ .

Although there is a significant excess, there could be deficiencies in our simplified halo model. Firstly, if the halo exhibits net pro-grade rotation, then our estimate for the halo fraction will be underestimated. However, to bridge the gap between the observed and mock halo distributions would require an unfeasibly high level of rotation; to increase our halo contribution by around 54%, which would bring it into agreement with the observed distribution, the halo would need to be rotating at around 35 km s^{-1} . Although some works have claimed such high levels of rotation may be possible (e.g. [Deason et al. 2011](#)), the general belief is that rotation should not be this large (e.g. [Allende Prieto et al. 2006](#); [Smith et al. 2009a](#); [Bond et al. 2010b](#); [Fermani & Schönrich 2013](#); [King et al. 2015](#)). The second potential deficiency in the halo model is the level of anisotropy. However, our model adopts the dispersions of [Smith et al. \(2009a\)](#) with spherical anisotropy parameter,

$$\beta = 1 - \frac{\sigma_\phi^2 + \sigma_\theta^2}{2\sigma_r^2} = 0.69, \quad (6)$$

which is at the radial end of the commonly assumed values (measurements of β typically range from around 0.4 to 0.6; [Smith et al. 2009a](#); [Williams & Evans 2015](#); [King et al. 2015](#); [Das & Binney 2016](#)). Therefore, although we concede that the halo model parameters could be tweaked in order to decrease the discrepancy between the predicted distributions of r_{peri} , such an approach is unlikely to completely reconcile the discrepancy.

If we accept that halo contamination may be present, one way to discriminate against this is to impose a metallicity cut, as we have discussed above. By restricting our sample to $[\text{Fe}/\text{H}] > -0.6$ we remove a large amount of the halo contamination (remember that the halo has a mean -1.46 dex and dispersion 0.3 dex; [Ivezić et al. 2008](#)) and should retain any Hills stars, which are expected to have high metallicities.

This reduces our sample considerably. The total number of spectra falls from 13,170 to 4,893 and the number of Hills candidates is only 10. Despite these small

numbers, we can repeat the above exercise and predict the distribution of r_{peri} for the halo. There are only 48 counter-rotating stars in this metallicity range, indicating that the halo fraction is around 1.0%. The resulting prediction for the halo r_{peri} distribution is shown by the black line in [Figure 7](#) and can be compared to the observed distribution in red. Here the agreement is much better, indicating that these stars are more consistent with being from the metal-rich tail of the halo population.

It is interesting to note the discrepancy between the two distributions in [Figure 6](#) is not reflected in the metal-rich sample in [Figure 7](#). For example, the full sample of Hills candidates has 77 stars with $r_{\text{peri}} < 0.5$ kpc, while our mock halo sample predicts only 50, but for the metal-rich sample only 2 stars remain with $r_{\text{peri}} < 0.5$ kpc. This leaves 25 metal-poor stars unaccounted for and, as mentioned above, we do not believe this can be explained by deficiencies in our halo model.

Two other possible sources of contamination are bulge and thick-disk stars on radial orbits, but neither of these are expected to be significant. As pointed out by [Vickers et al. \(2015\)](#), the bulge dispersion of around 100 km s^{-1} is insufficient to produce a significant number of stars in the solar neighborhood (note that our sample are predicted to have left the bulge with velocities in excess of 450 km s^{-1}). We estimate the thick disk contamination using the Besancon model [Robin et al. \(2003\)](#). This kinematics in this model are flawed in that it assumes a Gaussian profile for the azimuthal velocities, whereas in reality the asymmetric drift induces a skew in the distribution (see Section 4.8.2 of [Binney & Tremaine 2008](#)). To alleviate this issue, we replace Besancon's azimuthal velocity distribution with the physically-motivated distribution of [Schönrich & Binney \(2012\)](#). This model predicts negligible thick-disk contamination. Although it is not inconceivable that one thick-disk star may be present in our two samples, the chances of significant contamination is small. For example, for the full sample of 13,170 stars, the probability that we have one thick-disk star on a highly radial orbit ($r_{\text{peri}} < 0.5$ kpc) is 27%, but the probability that we have three or more is less than 1%. For the metal-rich sample of 4,893 stars, the probability of obtaining one radial thick-disk star is 8%, but less than 1% for two or more stars.

In conclusion, although our metal-rich Hills candidates appear to be consistent with predictions for halo contamination (albeit in some cases with unusually high metallicities), the metal-poor candidates are in conflict. While the nature of our Hills candidates is unclear, it is unlikely that the metal-poor candidates can be explained away by halo, bulge or disk contamination. One could argue that they are the tail of high velocity runaway stars, ejected from mechanisms other than an interaction with the supermassive black hole. However, assuming these stars originated in the bulge, our ejection velocities are all in excess of 400 km s^{-1} , which is hard to achieve by standard runaway mechanisms (see Section 1). The more metal-rich stars could potentially have been ejected from the disk, but this would require an ejection velocity vector orientated precisely against the disk's rotation in order to place the star on a highly radial orbit. This is possible, but the combination of (a) the requirement on the ejection vector, together with the fact that (b) such

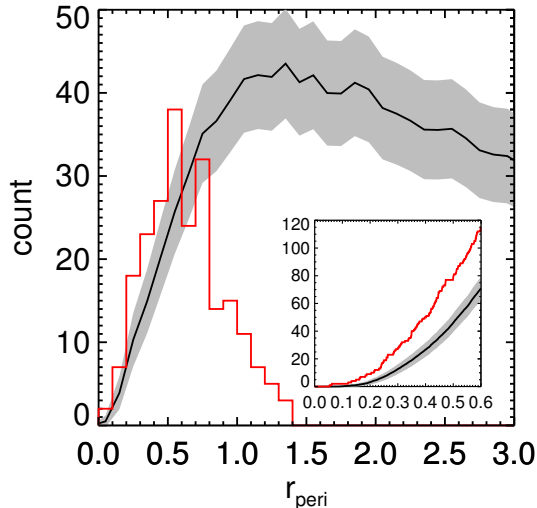


FIG. 6.— The distribution of the peri-centric radii for our full sample of Hills candidates (red line) and our mock halo stars (black line). The shaded region shows the 1σ uncertainty in the mock halo distribution, assuming Poissonian errors. The inset shows the cumulative distribution.

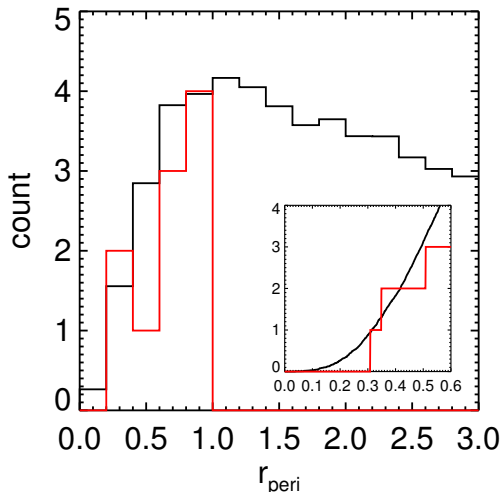


FIG. 7.— As Figure 6, but for our metal-rich sample of Hills candidates ($[\text{Fe}/\text{H}] > -0.6$).

ejection speeds are towards the tail of the predicted distribution, mean that we do not expect this to be a major source of contamination.

6. CONCLUSION

Stars ejected from the Galactic centre can be used to place important constraints on the Milky Way potential (e.g. [Gnedin et al. 2005](#)). Although many such stars have been found, most are too distant to obtain the detailed 6D phase-space information that is required to constrain the potential. We have therefore carried out a search for nearby ejected stars, focusing not only on unbound ejecta (hypervelocity stars) but also including bound ejecta (which we dub Hills stars). By integrating orbits back through time we have identified a number of candidates, with orbits consistent with Galactic centre ejection. Our analysis used data from SDSS and, since

the efficacy of such studies are often hampered by deficiencies in proper motion catalogs, we have chosen to utilize the reliable, high-precision Stripe 82 proper motion catalogue ([Bramich et al. 2008](#); [Koposov et al. 2013](#)).

From the 13,170 SDSS stellar spectra in Stripe 82, we found 226 candidate Hills stars. As was discussed in Section 5, this number is significantly in excess of what we would expect for halo stars on radial orbits and cannot be explained by disk or bulge contamination. Deficiencies in our halo model, due to incorrect assumptions about rotation or anisotropy, are unlikely to reconcile this discrepancy. One might speculate that an accretion event on a very radial orbit could cause this signal, but in conclusion the nature of the metal-poor candidates remains uncertain.

Since all known hypervelocity stars to-date are metal rich, we expect that our Hills candidates should also be metal rich. However, there is a selection bias at play, since hypervelocity stars have been identified based on the fact that they are young (and hence metal-rich) stars that stand out amongst the old populations of the Galactic halo. So it is possible that there may be low-mass metal-poor hypervelocity stars, but they have remained hidden from the existing search techniques. On the other hand, because the Galactic bulge was enriched on such a short time-scale, the fraction of metal-poor stars in the bulge will be small, even at earlier times. This indicates that it would be surprising if we were to find a significant population of metal-poor Hills stars. If we follow the assumption that Hills stars should be metal-rich and restrict ourselves to such stars, we find 29 candidates with $[\text{Fe}/\text{H}] > -0.8$ dex and 10 with $[\text{Fe}/\text{H}] > -0.6$ dex. Their metallicities are more consistent with what we expect for bulge ejecta, and so follow-up observations could be particularly interesting for these stars. It is worth noting that even if these are genuine Hills stars, none of them are unbound and hence our result is in agreement with the non-detection from [Kollmeier et al. \(2010\)](#).

We can carry out an order-of-magnitude estimate of the ejection rate for these candidates, following [Kollmeier et al. \(2010\)](#), see the first paragraph of Section 3.2). The survey volume of our 250 sq. deg. wedge is around 3.2 kpc^3 , assuming we probe distances of 0.5 to 5 kpc. However, from Table 1 we can see only 5.7% of stars have spectra, meaning that the effective volume is only 0.18 kpc^3 . This is equivalent to a thin Galacto-centric shell at 9 kpc of width $1.7 \times 10^{-4} \text{ kpc}$, which a 300 km/s Hills star will spend $5.7 \times 10^{-4} \text{ Myr}$ traversing. Therefore, if we assume we have between 1 to 10 Hills stars in our SDSS sample, this implies an ejection rate of $2 - 20 \times 10^3 \text{ Myr}^{-1}$. This is a very simplified calculation which neglects two important considerations: firstly, the survey volume we probe depends on the spectral type; and secondly, since our sample are all bound, they may not be on their first passage through the solar radius. Despite these limitations, our estimate is comparable to existing predictions; although classical B-type HVSSs are predicted to be ejected at a rate of 100 to 1000 Myr^{-1} (e.g. [Zhang et al. 2013](#)), [Kenyon et al. \(2008\)](#) calculate that the ejection rate of low-mass Hills stars could be around 2 to 3 orders-of-magnitude greater than that of B-type stars. Clearly larger samples with better statistics are required to fully address the question of ejection rates.

To address the issue of sample size, we have developed a technique using proper-motions to optimize candidate selection (Section 4). We have tested this approach with our own radial velocities obtained from the Palomar 200-inch telescope. This technique provides considerable improvement on the blind spectroscopic sample of SDSS, being able to identify Hills candidates with an efficiency around 20 times better than a blind search. We believe there is good potential for this approach in future. At 250 sq. deg., Stripe 82 covers less than 150th of the total sky. Current surveys, such as Pan-STARRS (Kaiser et al. 2010), could immediately be used to repeat this exercise for significantly larger volumes.

Clearly the efficacy of this method depends on the uncertainties in the observed quantities, most notably the distances and proper motions. The thickness of the disk crossing track in Figure 4 (see Section 4.1 determines how reliable our method is; if we knew all observed photometric properties to infinite precision, then this track would be a line and for bona-fide Hills stars this would intersect the GC. The Gaia mission will provide both distances and proper motions to exquisite precision for many millions of stars in the solar neighborhood, together with metallicities from the on-board spectro-photometry⁴ (Liu et al. 2012). Such a dataset would dramatically improve the efficacy of our method (see Fig. 8), producing a catalogue of high-probability candidates that could be followed up with moderate observing resources. The accurate distances and proper motions leads to much more precise knowledge of the ejected star’s orbit, consequently providing greatly improved constraints on the Galactic potential. We are now working on a follow-up paper to quantify how many Hills stars would be required to place meaningful constraints on the potential and this will be reported in due course.

ACKNOWLEDGMENTS

The authors wish to thank Alberto Rebassa-Mansergas, Matthew Molloy, Eric Peng, and Hengxiao Guo for assistance with this work, and Jinliang Hou and the cluster group at SHAO for useful discussions. This work is supported by the CAS One Hundred Talent Fund, NSFC Grants 11173002 & 11333003, the Strategic Priority Research Program The Emergence of Cosmological Structures of the Chinese Academy of Sciences (XDB09000000), the National Key Basic Research Program of China (2014CB845700) and the National Science Foundation grant AST 14-09421.

It uses data obtained through the Telescope Access Program (TAP), which has been funded by the Strategic Priority Research Program The Emergence of Cosmological Structures (Grant No. XDB09000000), National As-

tronomical Observatories, Chinese Academy of Sciences, and the Special Fund for Astronomy from the Ministry of Finance. Observations obtained with the Hale Telescope at Palomar Observatory were obtained as part of an agreement between the National Astronomical Observatories, Chinese Academy of Sciences, and the California Institute of Technology. Observations obtained

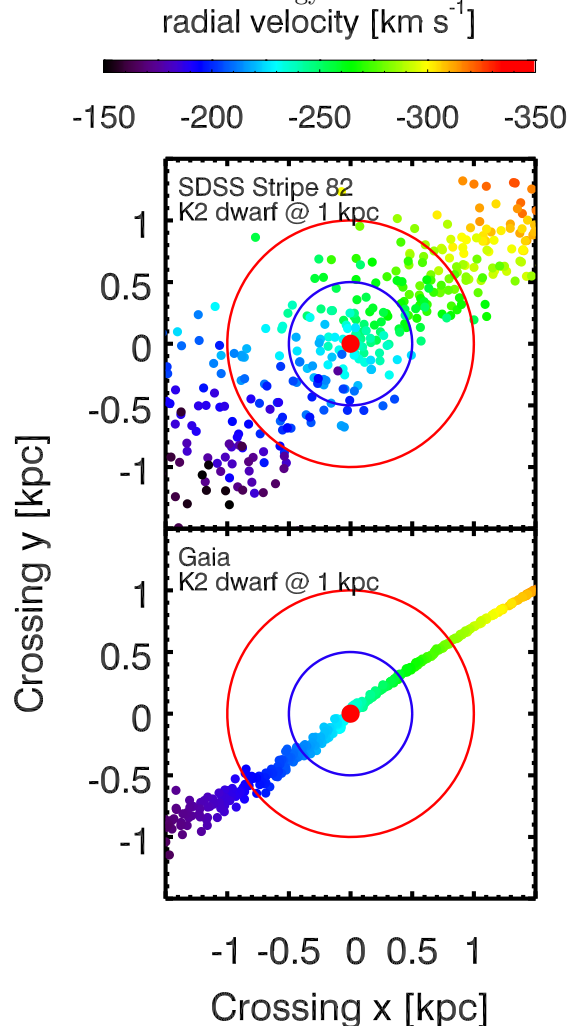


FIG. 8.— An illustration of how our proper motion selection technique will improve with forthcoming Gaia data. We show two disk crossing tracks for a hypothetical Hills star, assuming this is a K2-dwarf located at 1 kpc. The top panel shows typical Stripe 82 uncertainties (errors of 20% in distance and 1.5 mas/yr in proper motion), while the bottom panel shows projected end-of-mission Gaia errors (4.5% in distance and 0.02 mas/yr in proper motion).

with the Hale Telescope at Palomar Observatory were obtained as part of an agreement between the National Astronomical Observatories, Chinese Academy of Sciences, and the California Institute of Technology.

APPENDIX

ADDITIONAL HILLS CANDIDATES FROM SDSS SPECTROSCOPY

Here, in Figure 9, we present plots of the crossing position for the remaining Hills candidates from Table 2. The best nine candidates (i.e. with $[\text{Fe}/\text{H}] \geq -0.57$ dex) are presented in Fig. 3.

⁴ Although radial velocities will also be obtained, this is only for the brightest stars, obtaining accuracies of around 5 km s⁻¹ at $V \sim 14$ mag. See <http://www.cosmos.esa.int/web/gaia/science-performance> and de Bruijne (2012)

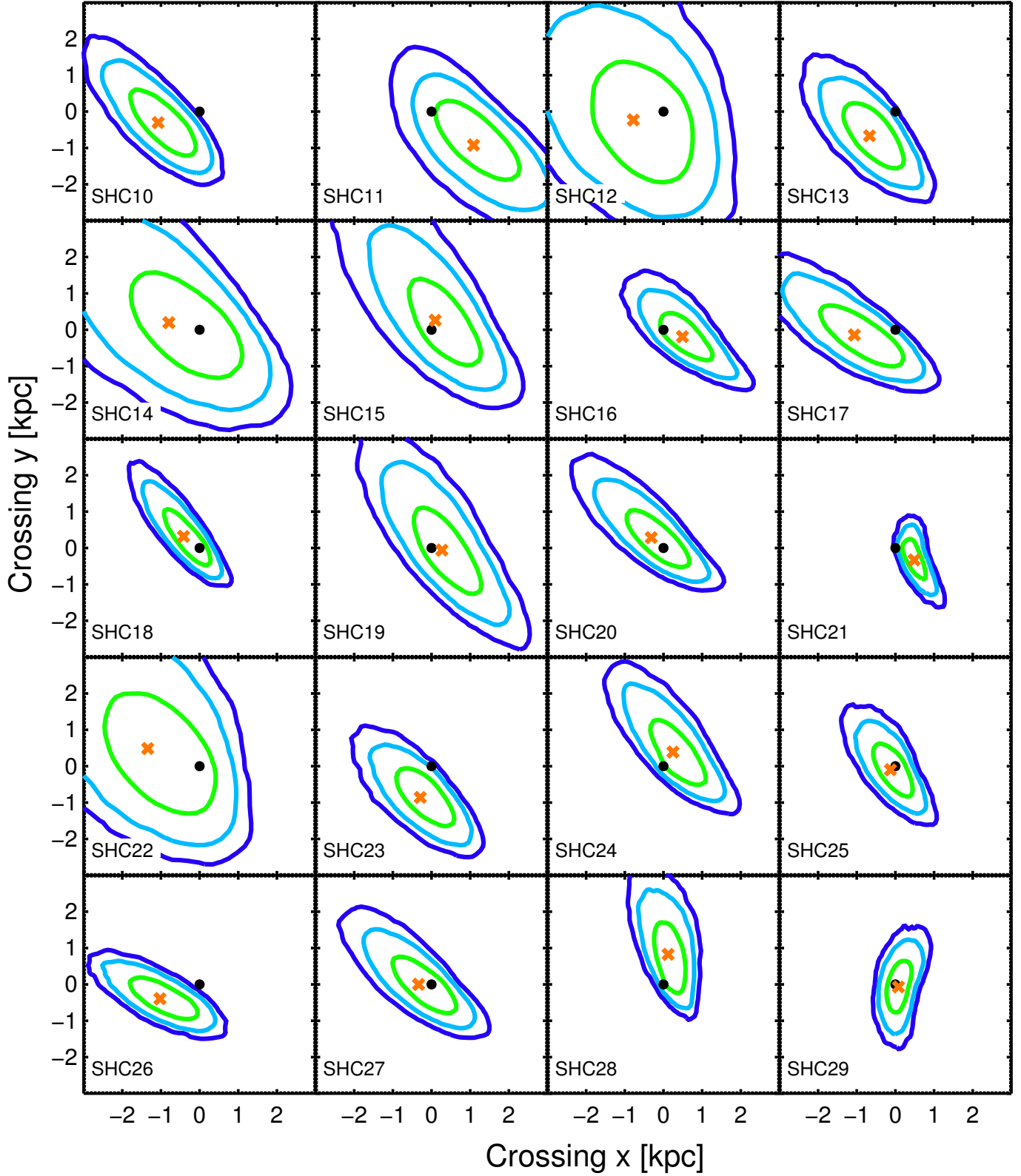


FIG. 9.— This figure shows the last disk crossing position for our moderately metal-rich SDSS Hills candidates (i.e. with $-0.8 \leq [Fe/H] \leq -0.59$ dex). The green, cyan and blue lines correspond to 1σ , 2σ and 3σ , respectively. The orange crosses show the crossing position if we do not account for observational errors. The black dot shows the position of Galactic center. The nine most metal-rich candidates are presented in Fig. 3.

REFERENCES

- Abazajian, K. N., Adelman-McCarthy, J. K., Agüeros, M. A., et al. 2009, *ApJS*, 182, 543
- Allende Prieto, C., Beers, T. C., Wilhelm, R., et al. 2006, *ApJ*, 636, 804
- Allende Prieto, C., Sivarani, T., Beers, T. C., et al. 2008, *AJ*, 136, 2070
- Annis, J., Soares-Santos, M., Strauss, M. A., et al. 2014, *ApJ*, 794, 120
- Binney, J., & Tremaine, S. 2008, *Galactic Dynamics: Second Edition* (Princeton University Press)
- Blaauw, A. 1961, *Bull. Astron. Inst. Netherlands*, 15, 265
- Bond, N. A., Ivezić, Ž., Sesar, B., et al. 2010a, *ApJ*, 716, 1
- , 2010b, *ApJ*, 716, 1
- Boubert, D., & Evans, N. W. 2016, *ArXiv e-prints*, [arXiv:1606.02548](https://arxiv.org/abs/1606.02548)
- Bramich, D. M., Vidrih, S., Wyrzykowski, L., et al. 2008, *MNRAS*, 386, 887
- Brown, W. R. 2015, *ARA&A*, 53, 15
- Brown, W. R., Geller, M. J., & Kenyon, S. J. 2014, *ApJ*, 787, 89
- Brown, W. R., Geller, M. J., Kenyon, S. J., & Kurtz, M. J. 2005, *ApJ*, 622, L33
- Burstein, D., Faber, S. M., Gaskell, C. M., & Krumm, N. 1984, *ApJ*, 287, 586
- Carlin, J. L., Casetti-Dinescu, D. I., Grillmair, C. J., Majewski, S. R., & Girard, T. M. 2010, *ApJ*, 725, 2290
- Carlin, J. L., Grillmair, C. J., Muñoz, R. R., Nidever, D. L., & Majewski, S. R. 2009, *ApJ*, 702, L9
- Carlin, J. L., Majewski, S. R., Casetti-Dinescu, D. I., et al. 2012, *ApJ*, 744, 25
- Das, P., & Binney, J. 2016, *ArXiv e-prints*, [arXiv:1603.09332](https://arxiv.org/abs/1603.09332)
- de Bruijne, J. H. J. 2012, *Ap&SS*, 341, 31
- Deason, A. J., Belokurov, V., & Evans, N. W. 2011, *MNRAS*, 411, 1480
- Dehnen, W., & Binney, J. 1998, *MNRAS*, 294, 429
- Faber, S. M., Friel, E. D., Burstein, D., & Gaskell, C. M. 1985, *ApJS*, 57, 711
- Fermani, F., & Schönrich, R. 2013, *MNRAS*, 432, 2402
- Gies, D. R. 1987, *ApJS*, 64, 545
- Gnedin, O. Y., Gould, A., Miralda-Escudé, J., & Zentner, A. R. 2005, *ApJ*, 634, 344
- Gorgas, J., Faber, S. M., Burstein, D., et al. 1993, *ApJS*, 86, 153
- Hills, J. G. 1988, *Nature*, 331, 687
- Ivezić, Ž., Sesar, B., Jurić, M., et al. 2008, *ApJ*, 684, 287
- Jurić, M., Ivezić, Ž., Brooks, A., et al. 2008, *ApJ*, 673, 864
- Kaiser, N., Burgett, W., Chambers, K., et al. 2010, in *Proc. SPIE*, Vol. 7733, *Ground-based and Airborne Telescopes III*, 77330E
- Kenyon, S. J., Bromley, B. C., Brown, W. R., & Geller, M. J. 2014, *ApJ*, 793, 122
- Kenyon, S. J., Bromley, B. C., Geller, M. J., & Brown, W. R. 2008, *ApJ*, 680, 312
- King, III, C., Brown, W. R., Geller, M. J., & Kenyon, S. J. 2015, *ApJ*, 813, 89
- Kollmeier, J. A., & Gould, A. 2007, *ApJ*, 664, 343
- Kollmeier, J. A., Gould, A., Rockosi, C., et al. 2010, *ApJ*, 723, 812
- Koposov, S. E., Belokurov, V., & Wyn Evans, N. 2013, *ApJ*, 766, 79
- Le Borgne, J., Bruzual, G., Pelló, R., et al. 2003, *A&A*, 402, 433
- Lee, Y. S., Beers, T. C., Sivarani, T., et al. 2008a, *AJ*, 136, 2022
- , 2008b, *AJ*, 136, 2022
- Li, Y., Luo, A., Zhao, G., et al. 2012, *ApJ*, 744, L24
- Liu, C., Bailer-Jones, C. A. L., Sordo, R., et al. 2012, *MNRAS*, 426, 2463
- McMillan, P. J. 2011, *MNRAS*, 414, 2446
- Moutaka, J., Ilovaisky, S. A., Prugniel, P., & Soubiran, C. 2004, *PASP*, 116, 693
- Oke, J. B., & Gunn, J. E. 1982, *PASP*, 94, 586
- Palladino, L. E., Schlesinger, K. J., Holley-Bockelmann, K., et al. 2014, *ApJ*, 780, 7
- Perets, H. B., & Šubr, L. 2012, *ApJ*, 751, 133
- Piffl, T., Scannapieco, C., Binney, J., et al. 2014, *A&A*, 562, A91
- Portegies Zwart, S. F. 2000, *ApJ*, 544, 437
- Poveda, A., Ruiz, J., & Allen, C. 1967, *Boletín de los Observatorios Tonantzintla y Tacubaya*, 4, 86
- Quinn, D. P., & Smith, M. C. 2009, *MNRAS*, 400, 2128
- Ramspeck, M., Heber, U., & Edelmann, H. 2001, *A&A*, 379, 235
- Robin, A. C., Reylé, C., Derrière, S., & Picaud, S. 2003, *A&A*, 409, 523
- Rossi, E. M., Kobayashi, S., & Sari, R. 2014, *ApJ*, 795, 125
- Sánchez-Blázquez, P., Peletier, R. F., Jiménez-Vicente, J., et al. 2006, *MNRAS*, 371, 703
- Schiavon, R. P. 2007, *ApJS*, 171, 146
- Schlegel, D. J., Finkbeiner, D. P., & Davis, M. 1998, *ApJ*, 500, 525
- Schönrich, R. 2012, *MNRAS*, 427, 274
- Schönrich, R., & Binney, J. 2012, *MNRAS*, 419, 1546
- Sesar, B., Ivezić, Ž., Lupton, R. H., et al. 2007, *AJ*, 134, 2236
- Smith, M. C., Okamoto, S., Yuan, H.-B., & Liu, X.-W. 2012, *Research in Astronomy and Astrophysics*, 12, 1021
- Smith, M. C., Wyn Evans, N., & An, J. H. 2009a, *ApJ*, 698, 1110
- Smith, M. C., Ruchti, G. R., Helmi, A., et al. 2007, *MNRAS*, 379, 755
- Smith, M. C., Evans, N. W., Belokurov, V., et al. 2009b, *MNRAS*, 399, 1223
- Stone, R. C. 1991, *AJ*, 102, 333
- Tauris, T. M. 2015, *MNRAS*, 448, L6
- Tetzlaff, N., Neuhauser, R., & Hohle, M. M. 2011, *MNRAS*, 410, 190
- Vickers, J. J., Smith, M. C., & Grebel, E. K. 2015, *AJ*, 150, 77
- Vidrih, S., Bramich, D. M., Hewett, P. C., et al. 2007, *MNRAS*, 382, 515
- Watkins, L. L., Evans, N. W., Belokurov, V., et al. 2009, *MNRAS*, 398, 1757
- Williams, A. A., & Evans, N. W. 2015, *MNRAS*, 454, 698
- Worthey, G., Faber, S. M., Gonzalez, J. J., & Burstein, D. 1994, *ApJS*, 94, 687
- Yanny, B., Rockosi, C., Newberg, H. J., et al. 2009, *AJ*, 137, 4377
- Zhang, F., Lu, Y., & Yu, Q. 2013, *ApJ*, 768, 153
- Ziegerer, E., Volkert, M., Heber, U., et al. 2015, *Å*, 576, L14